ACS NANO

www.acsnano.org

Article

Bidisperse Nanospheres Jammed on a Liquid Surface

Yige Gao,[⊥] Paul Y. Kim,[⊥] David A. Hoagland,[*] and Thomas P. Russell[*]

Cite This: *ACS Nano* 2020, 14, 10589−10599

Read Online

ACCESS | Metrics & More | Article Recommendations | Supporting Information

ABSTRACT: Jammed packings of bidisperse nanospheres were assembled on a nonvolatile liquid surface and visualized to the single-particle scale by using an *in situ* scanning electron microscopy method. The PEGylated silica nanospheres, mixed at different number fractions and size ratios, had large enough in-plane mobilities prior to jamming to form uniform monolayers reproducibly. From the collected nanometer-resolution images, local order and degree of mixing were assessed by standard metrics. For equimolar mixtures, a large-to-small size ratio of about 1.5 minimized correlated metrics for local orientational and positional order, as previously predicted in simulations of bidisperse disk jamming. Despite monolayer uniformity, structural and depletion interactions caused spheres of a similar size to cluster, a feature evident at size ratios above 2. Uniform nanoparticle monolayers of high packing disorder are sought in many liquid interface technologies, and these experiments outlined key design principles, buttressing extensive theory/simulation literature on the topic.

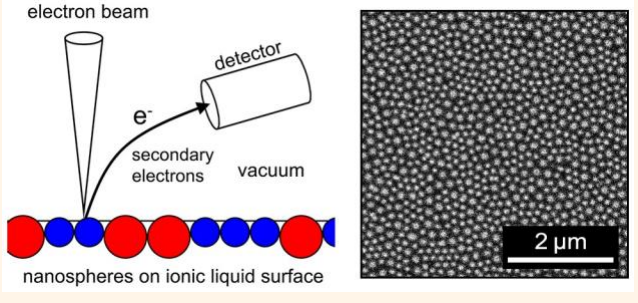

KEYWORDS: *electron microscopy, condensed matter, interfacial jamming, nanoparticles, ionic liquid*

Brought to high density, disordered materials such as colloidal suspensions and granular powders jam when internal, compressive load-bearing paths impede further densification and structural ordering.[1] In many surface and membrane applications, nanoparticle (NP) jamming provides an effective means to stabilize liquid interfaces and control their order/disorder.[2] Supporting high in-plane stiffness, disorder minimizes in-plane directionality and large-scale heterogeneities, properties beneficial for mechanically stabilized liquid interfaces.[3] However, rather than jamming with high disorder, dense monodisperse spheres and disks on a liquid interface tend to crystallize. Ellipsoidal particles do not crystallize as readily,[4] but they are harder to prepare and disperse than spheres. The mixing of two different sized spheres offers a more practical way to achieve a dense, uniform, and disordered particle packing on a liquid interface. Here, this bidisperse sphere strategy is explored for interfacial NP monolayers visualized to single particle resolution by scanning electron microscopy (SEM).

Simulations predict that the size disparity of a bidisperse sphere/disk mixture strongly affects the disorder in the corresponding two-dimensional (2D) dense packing.[5,6] For bidisperse spheres/disks of radii a_1 and a_2 (with $a_1 < a_2$), the extent of disorder minimally depends on the ratio of radii $\sigma = a_2/a_1$, the number fraction of small sphere/disk n, and the overall areal fraction ϕ. Additional variables, such as the interparticle interaction potential(s) and the size polydispersities of the two sphere/disk populations, may also come into play. The 2D packing of bidisperse spheres/disks has been treated in numerous theoretical/simulation efforts, but the corresponding experimental literature is sparse, especially for packings produced on a liquid interface, the 2D context of greatest practical interest.[7−9] Bocquet *et al.* simulated 2D mixtures of bisperse disks at $n = 0.5$ and noted that disorder markedly increases for $\sigma > 1.28$,[10] and likewise, Perera and Harrowell showed that a soft disk mixture of the same n and $\sigma \sim 1.40$ forms a stable glass.[11] Speedy computed the glass transition of hard disk mixtures, finding that eutectic glasses form at $\sigma \sim 1.40$.[12] Russo *et al.* interpolated between crystal- and glass-forming behaviors and showed that the ability to form glass is signaled by a depression of the melting points toward the eutectic points.[13]

By simulations, Koeze *et al.* mapped the 2D jamming of bidisperse disks of varied n and σ onto the critical areal fraction ϕ_c at the onset of jamming.[14] They predicted local minima of

Received: June 4, 2020
Accepted: August 6, 2020
Published: August 6, 2020

https://dx.doi.org/10.1021/acsnano.0c04682
ACS Nano 2020, 14, 10589−10599

order not just around the previously known condition $n \sim 0.50$ and $\sigma \sim 1.40$ but also near $n \sim 0.20$ and $\sigma \sim 2.50$.

Compared to larger colloidal particles, NPs decorated with stabilizing ligands on liquid interfaces show larger in-plane mobilities and weaker in-plane interactions, properties that favor jamming relative to irreversible aggregation. NP mixtures can reach a steady state rapidly by thermal diffusion without forming irreversible aggregates due to their weak pair interactions. The same properties also amplify opportunities for unjammed NP mixtures to phase separate via the action of depletion interactions. This type of phase separation in 2D and three-dimensional (3D) sphere mixtures has received considerable attention, but less so for the small σ values cited above[15] and, to our knowledge, never for NPs attached on a liquid surface or packed to an areal density that approaches jamming. Further, different from the case of larger particles, the ligand size for NPs can approach and even exceed the particle size, making NP interactions more sensitive to ligand identity, length, and density.[16] For a properly designed bidisperse system, tracking individual NPs on a liquid surface should provide insights into jamming and vitrification processes under conditions dominated by random thermal motion and hard sphere repulsions. On a practical level, disordered interfacial NP layers are desired, for example, to stabilize Pickering emulsions and structure liquids.[17]

Several advanced optical microscopy methods can visualize NPs in liquids,[18] and while these methods can identify single NPs in isolation, they cannot resolve and track single NPs in a dense assembly.[19] Turning to electron microscopy, which has higher resolution, specimens solvated with ordinary liquids must be sealed against instrument vacuum inside a closed, windowed cell.[20] Such cells are suited only to transmission electron microscopy (TEM), and the examination of liquid specimens and interfaces is potentially compromised by the physical and chemical constraints of the cell (i.e., window gap ~50−100 nm, potentially strong interactions between NPs and windows, *etc*.). To overcome these shortcomings, we developed an *in situ* scanning electron microscopy (SEM) method that employs nonvolatile ionic liquids (ILs) as NP-dispersing media.[21] An experimental SEM schematic is displayed in Figure 1. Our approach enables an easy imaging

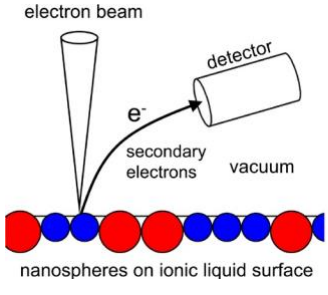

$2a_1$	$2a_2$	σ
144	187	1.29
144	195	1.35
121	187	1.54
121	195	1.61
100	195	1.95
80	195	2.43

Figure 1. SEM imaging of a bidisperse NP monolayer. Experimental schematics and NP pairings used to make bidisperse mixed NP monolayers. Radii a_1 and a_2 are in nm.

of "open" specimens, *i.e.*, those with liquid interfaces directly exposed to instrument vacuum. Electron doses and voltages are lower than for TEM, reducing artifacts arising from charging and heating.[22] At optimized conditions, NP features and positions on a liquid interface can be obtained at ~5 nm resolution across a > 300 μm^2 area containing >8000 closely packed NPs. Further, the positions of individual NPs in such packings can be tracked for lengthy times (~60 min or longer) from images collected at several frames/second.

This report considers how dense packing of bidisperse, PEGylated silica NPs on an IL surface varies with n and σ. Since ~10 nm diameter NPs of truly narrow relative size distribution are unavailable ("relative" defined by reference to the average NP diameter), we directed attention at NPs of larger diameter, ~80−200 nm, which afford narrower relative size distributions and greater SEM contrast. Because their diameters were all below the ~250 nm diffraction limit of light, these NPs and their packed assemblies could not be resolved to the single particle level by optical microscopy. SEM had no difficulties in resolving individual particles, even when they were in contact with each other. The in-plane interactions measured between two isolated NPs conformed well to expectation for ideal hard spheres, and interfacial binding energies were large, reaching hundreds of k_BT per NP.[16] Such binding energies led spontaneously to IL surfaces sufficiently saturated with NPs to jam at high ϕ. Important features of the model NP−liquid system, such as contact angle, binding energy, and pair interaction potential, were characterized in prior work.[16]

From NP positions obtained by SEM, structural analyses of the jammed states were performed to obtain various order and mixing metrics, allowing for direct comparisons of the experimental results to predictions from previous simulations/theories for 2D sphere/disk mixing and jamming. These parameters characterize local orientational and positional order, number of nearest neighbors, and randomness of local mixing. In no instance was macrophase separation noted, but under some conditions of n and σ, large and/or small spheres formed small clusters, influencing the mixing and jamming metrics calculated. Whether such clustering reflected a fully equilibrated mixture or just an intermediate kinetically trapped state remains undetermined. In future work, to address such questions, the dynamics of jamming will be explored using the SEM method's ability to track individual NPs before, during, and after jamming.

RESULTS AND DISCUSSION

Characterization, Attachment, and Imaging of NPs.

As a consequence of their sol−gel synthesis, silica NPs can display nanoscale surface roughness and finite size polydispersity.[23] TEM performed on NPs prior to ligand attachment showed essentially no shape eccentricity and little indication of surface roughness. The TEM-determined coefficient of size variation CV, defined as $s/a \times 100$, where a and s are the respective mean and standard deviation of NP radius, decreased from ~7% to ~4% as a increased from ~40 to ~100 nm. To minimize impacts of CV on NP packing, pairings were selected such that $\sigma > 1.20$. The six pairings investigated here, along with their associated σ, are summarized in Figure 1. The ligand layer thickness, as estimated by the radius of gyration of free 5000 g/mol PEG in a theta solvent, was ~3−5 nm,[24] which is small but not negligible compared to the NP radii. No account of ligand thickness is made in specifying σ and ϕ since PEG's ligand conformation is unknown. For the low ligand molecular weight PEG chosen, the intramolecular excluded volume contribution to free coil size is anticipated to be insignificant, and for the low ligand grafting densities

https://dx.doi.org/10.1021/acsnano.0c04682
ACS Nano 2020, 14, 10589−10599

achieved, the same is likely true for the intermolecular contribution to ligand stretching.

https://dx.doi.org/10.1021/acsnano.0c04682
ACS Nano 2020, 14, 10589−10599

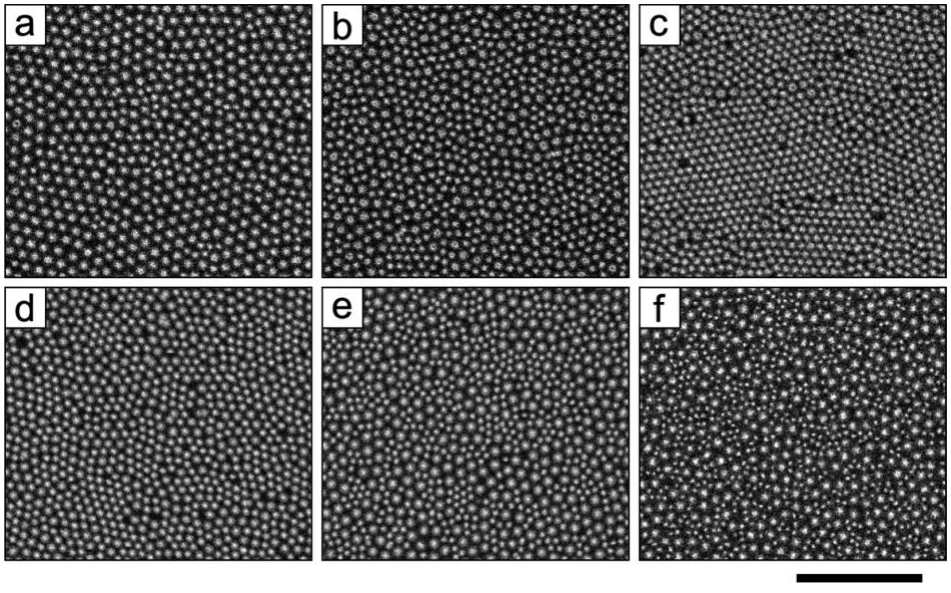

Figure 2. SEM images of bidisperse NP packings on an IL surface. (a) $\sigma = 1.35$, $n = 0.24$, $\phi = 0.74$; (b) $\sigma = 1.35$, $n = 0.63$, $\phi = 0.75$; (c) $\sigma = 1.35$, $n = 0.93$, $\phi = 0.80$; (d) $\sigma = 1.29$, $n = 0.59$, $\phi = 0.78$; (e) $\sigma = 1.61$, $n = 0.60$, $\phi = 0.75$; and (f) $\sigma = 1.95$, $n = 0.64$, $\phi = 0.69$. Scale bar is 2 μm.

The difference in surface energy between PEG and IL (1-ethyl-3-methylimidazolium ethylsulfate), 43 mJ/m^2 vs. 48 mJ/m^2, respectively, drove formation of NP monolayers by ligand adsorption to the IL surface. The growth of NP monolayers at the initial stage was observed *in situ* as shown in Figure S1 in the Supporting Information. The ligands also led to good dispersibility of the NPs in methanol and IL, with no perceptible NP aggregation observed for several months. Pendant drop tensiometry showed that the IL−air interfacial binding energy for ~100−200 nm PEGylated silica NPs was ~500 to ~2000 k_BT,[16] sufficient to achieve almost irreversible NP anchoring to the liquid surface. Over dozens of SEM experiments conducted under ordinary imaging conditions, with tens of thousands of NPs observed, none were seen to detach into the bulk. Similarly, no contacting NPs on the surface were observed to aggregate irreversibly unless the adsorbed NP monolayer was held in a compressed state for many hours. (Such compression was not part of the protocol applied here.)

SEM, when operated at 3 kV accelerating voltage, discerns features within ~20 nm of the IL surface.[21] Under this condition, the low NP-IL-vacuum contact angle, ~14°, made each NP appear as a circular "cap" of radius smaller than the physical NP radius, with a greater portion of the NP residing well beneath the IL surface.[16] Thus, direct contacts between NPs were not observed by SEM, since they occurred below the surface out of view. The low measured contact angle reflected the favorable interactions of the polar PEG ligands with the polar IL. Beyond hard core repulsion, an attractive interaction with a well depth ~0.1 k_BT was observed at NP separations of order the NP radius and tentatively ascribed to capillary NP interactions arising from a ligand-induced meniscus surrounding each NP; potential sources of the attraction are discussed in our prior work.[16] This attraction was too weak to have meaningful consequences. Rapid Brownian motion of individual NPs was observed by SEM even when ϕ was only slightly below jamming. The NPs effectively interacted with each other

Irrespective of radii, the irreversible adsorption of NPs led to an intermediate time (tens of minutes to several hours) saturation at $\phi = 0.75 \pm 0.05$, calculated as $\pi(a_1^2 N_1 + a_2^2 N_2)/$ as 2D hard spheres/disks.[16]

https://dx.doi.org/10.1021/acsnano.0c04682
ACS Nano 2020, 14, 10589−10599

A, where N_1/A and N_2/A are the areal number densities of small and large NP, respectively. This saturation level is considerably less than the $\phi \approx 0.91$ limit for a perfect 2D crystal of monodisperse hard spheres/disks, but this higher limit could experimentally be approached for monodisperse NPs by very slow interface compression and possibly by more extended annealing (not observed). The areal densities at saturation were well beyond the onset of local ordering ($\phi \sim 0.69$ for monodisperse NPs) but less than the threshold for collective jamming ($\phi \sim 0.86-0.88$ for monodisperse NPs) predicted by Torquato *et al.* through 2D disk simulations.[25,26] While ϕ at saturation was clearly affected by numerous packing imperfections, a failure to account in ϕ for the increase of NP radius by ligands was also a factor. If ϕ at saturation is at $\phi \approx 0.86$, effective NP radii only about 6% larger than the bare radii are needed. The difference between bare and effective radii can be explained in terms of the thickness of the ligand shell on the NP surface.

Imaging of NP Mixtures. Figure 2 shows SEM micrographs of interfacial NP mixtures for several combinations of n and σ. The ~15 μm span of each micrograph is small enough relative to the ~3 mm IL drop radius that the imaged areas, located near the drop crests, were effectively flat. Due to their higher electron scattering contrast, the well-resolved NPs appear brighter than the background IL, and the large and small NPs, despite the dense packing, are readily distinguished from each other. The radius and intensity recorded across an image for each NP constituent were nearly uniform, indicating that NP vertical positions relative to the liquid surface did not fluctuate significantly. This conclusion was reinforced by a lack of significant change in NP intensity over time for images collected at one spot. The imaged radii are less than the NP physical radii, as was explained above, and the minimum center-to-center distance for like-sized NPs, when crowded into contact, corresponded well to the NP diameter. Centers of

https://dx.doi.org/10.1021/acsnano.0c04682
ACS Nano 2020, 14, 10589−10599

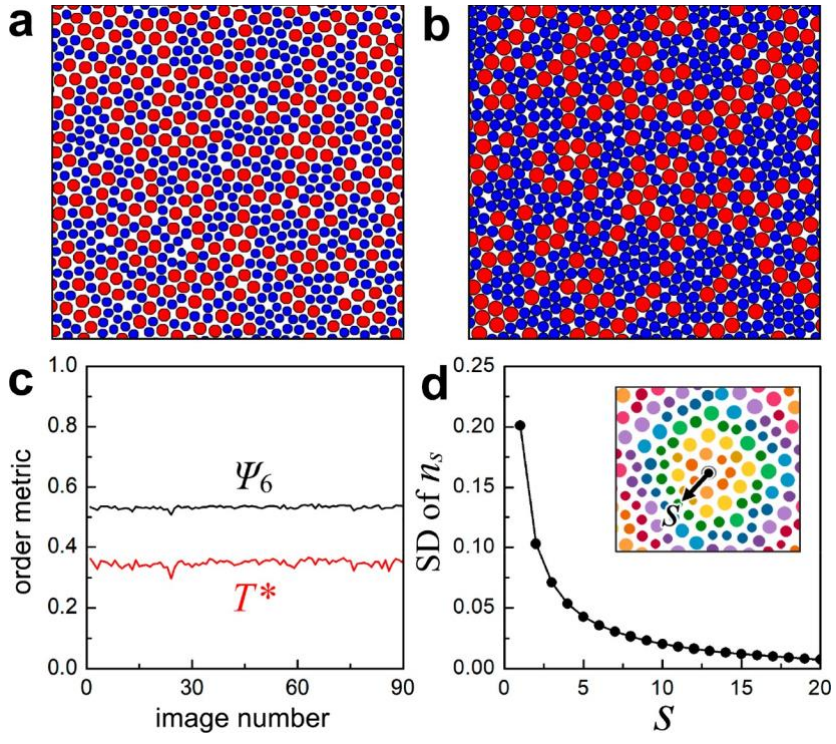

Figure 3. Assessments of jammed bidisperse NP packings. (a) Binarized image colorized according to NP size for σ = 1.35 and n = 0.63 [same conditions as Figure 2b]. (b) MRJ disk packing for σ = 1.40 and n = 0.75 (replotted a packing configuration simulated by Zachary *et al.*[28]). (c) Order metrics Ψ_6 and T^* evaluated at 90 image locations across the IL surface. (d) SD plotted against S for σ = 1.35 and n = 0.81 [same conditions as Figure 2c]. The inset to (d) shows an overview of how n_S was calculated as a function of S.

the small and large NPs probably did not lie in the same horizontal plane, but since σ was not too large, depths of their centers below the surface were similar. As calculated from the geometry sketched in Figure S2, the apparent radii of small and large NPs in their plane of mutual contact decrease proportionately with increasing size disparity (the sketch is for equal wetting angles of ~14°, the angles experimentally measured). For size ratios smaller than ~1.5, the radii are reduced by less than 2%, small enough for little influence on packing structures, although a precise calculation of its impact would be difficult. Hence, to simplify packing analyses, all NP centers were assumed to lie in the same plane. Unless externally perturbed, NPs always packed into uniformly dense monolayers that lacked large vacancies or wrinkles. After surface saturation, NP positions and packing did not change detectably over hours of SEM imaging, demonstrating that the NPs were effectively jammed; mean square displacements of NPs were within instrumental error ($<10^{-7}$ μm/s).

2D Packing of Bidisperse NP Mixtures. Figure 2a−c shows raw SEM images for σ = 1.35 mixtures at n = 0.24, 0.63, and 0.93. When n departed significantly from 0.5, *e.g.*, Figure 2a and c, the large or small majority NPs mostly packed into finite crystal-like domains in which the minority NPs were distributed as occasional substitutional defects. The rest of the minority NPs concentrated in disordered regions surrounding the majority NP domains. While the disorder in Figure 2c is slightly less than in Figure 2a, the disorder in Figure 2b, with n closer to 0.5, is much greater. Indeed, no clearly defined domains of order can be recognized. Previous jamming simulations found that such near-equal n mixtures with σ in the range 1.3−1.5 are almost fully disordered.[11,12,27] Figure 2d−f show the typical packing of bidisperse NPs of near-equal

https://dx.doi.org/10.1021/acsnano.0c04682
ACS Nano 2020, 14, 10589−10599

n for σ = 1.29, 1.61, and 1.95. With growing σ, the coordination number z (number of nearest neighbors) increasingly deviated from six (upward for the larger NP and downward for the smaller), impeding crystallization and inducing greater disorder. Only Figure 2d, below the nominal σ threshold for disorder cited above, suggests ordered domains. More detailed analyses of order and mixing are provided later.

Uniformity and Reproducibility of NP Mixing and Order. With interactions beyond hard core repulsion negligible, and with 2D mobility significant throughout monolayer assembly, the nominally jammed NP structures observed after several minutes were in a statistical sense both reproducible and well-defined. Average configurational properties were little sensitive to preparation details or mild external perturbations. Nonetheless, jammed monolayers did not find the lowest free energy state, and with suitable slow compression/annealing, at least some jammed configurations seemed able to undergo further densification and/or crystallization from the imaged, "kinetically trapped" state. Nonetheless, with monolayers not externally perturbed, any aging or densification processes occurred at times well beyond the tens of minutes to several hours accessible to the SEM experiment; for practical reasons, monolayers could not be monitored in the SEM for days or longer.

Figure 3a presents a binarized and colorized rendition of Figure 2b for comparison to Figure 3b, a literature simulation of bidisperse disks coupled through hard sphere interactions and packed at maximally random jamming (MRJ).[28] For the experiment, σ = 1.35, n = 0.63, and ϕ = 0.75, and for the simulation σ = 1.40, n = 0.75, and ϕ = 0.85. The experimental and simulated images are similar, and notably, although global disorder dominates, short-and medium-range packing correla-

https://dx.doi.org/10.1021/acsnano.0c04682
ACS Nano 2020, 14, 10589−10599

tions are suggested in both contexts, with extended clusters of small (blue) particles surrounded by extended clusters of large (red) particles.

According to theory and experiment, under depletion interactions, a $\sigma > 5$ bidisperse sphere mixture in three dimensions can macroscopically phase separate, either into two disordered phases or into a disordered and a crystalline phase.[29,30] In this 2D study, with $\sigma < 2.5$, such separation was not expected. Nevertheless, specimens could display spatial nonuniformity if mixing prior to jamming was incomplete. Therefore, to assess macroscopic uniformity, ~100 images were collected at different specimen locations, and for small, large, and all NPs composition parameters n and ϕ along with the bond-orientational order metric Ψ_6 and the translational order metric T^* (defined later) were plotted against image number, the latter in Figure 3c and the former in Figure S3. These plots demonstrate that NP mixing and order are essentially independent of location, leading to the reasonable conclusions that mixing was globally uniform and macroscopic phase separation was absent.

Local Mixing. At short length scales, random mixing in a jammed sphere/disk packing can be interrupted by the finite sizes of constituents, potentially generating nonuniformities of the type seen in Figure 3a, b.[31] To characterize these effects, n was calculated around each NP over areas of increasing radius, i.e., shell number S as defined by radical Voronoi tessellation, and the average n over these areas, dependent on S, was denoted n_S; each S is illustrated in Figure S4. This parameter measures how the small/large identity of a central NP locally perturbs mixture composition. The analysis is overviewed in inset of Figure 3d for packing conditions identical to those in Figure 3a; the inset shows a blackened central NP surrounded by NPs colored according to S and tinted to distinguish small from large NPs. Figure 3d plots the standard deviation (SD) of n_S against S, and SD was found to be largest when S equals unity, manifesting that the greatest mixing nonuniformity was at the shortest mixture length scale. SD decreased with increasing S, consistent with an increasingly uniform NP population, and by $S = 20$, SD was almost zero; the histograms of n_S became narrower with increasing S as shown in Figure S5. The observed length scale for random NP mixing, ~10 NP diameters, captures the apparent cluster size noted in Figure 3a. The magnitudes and sizes for clustering seem remarkably large for a local packing phenomenon. Other mixing analyses, such as the Fourier transform of the local perturbation in n, lead to an analogous smallest length scale for uniform mixing. For perfectly random mixtures, the probability of filling each shell with N particles with a small NP number fraction n has a binomial distribution. To examine random mixing of NPs, the curves in Figure S5 are fit with the probability density function (PDF) of the normal distribution, which can be used as an approximation to the binomial distribution for a sufficiently large N, *i.e.* $Nn(1-n)>3$;[32] N was larger than ~18 when $S \geq 2$. The PDF matched well for $S \geq 3$ in Figure S6, revealing random mixing at a length scale of several NP diameters.

Radial Distribution Functions and Order Metrics. Figure 4a–d shows the radial distribution functions $g(r)$ for $\sigma = 1.35$ (144 and 195 nm NPs) as n varies from 0.24 to 0.93. With each function manifesting translational order differently, four $g(r)$ functions are offered: correlation between pairs of any size, designated $g_0(r)$ (Figure 4a); between NPs of small radius, designated $g_{11}(r)$ (Figure 4b); between NPs of small and large radius, designated $g_{12}(r)$ (Figure 4c; identical by symmetry to $g_{21}(r)$); and between NPs of large radius, designated $g_{22}(r)$ (Figure 4d). These correlations are interrelated by $g_0(r) = n^2 g_{11}(r) + 2n(1-n)g_{12}(r) + (1-n)^2 g_{22}(r)$. Hence, integrated peaks of $g_0(r)$ are determined by n and relative peak intensities. The first peaks of $g_{11}(r)$, $g_{12}(r)$, and $g_{22}(r)$ arise from NPs in contact and lie at approximate r positions of $2a_1$, $a_1 + a_2$, and $2a_2$, respectively; although these peaks are slightly broadened by size polydispersity and experimental resolution, their positions are independent of n and σ due to hard-sphere like interactions. The same peaks appear in g_0(r), and as n increases, the largest peak shifts from $2a_2$ to a_1+a_2 and then to $2a_1$, expressing the change in the dominant NP pairing. At $n \sim 0.5$, the number of mixed pairs (captured in the magnitude of the second peak of $g_0(r)$) exceeds the number of unmixed pairs (captured in the magnitudes of the first and third peaks), and due to the larger disorder induced by the mixed pairings the peaks in $g_0(r)$ become broader and weaker. For n much larger or much smaller than ~0.5, peaks in $g_0(r)$ associated with the prevalent triangular lattice (at relative positions $\sqrt{1}$, $\sqrt{3}$, $\sqrt{4}$, $\sqrt{7}$...) evolve to the peak positions of either $g_{11}(r)$ or $g_{22}(r)$, although some overlap is seen with peaks contributed from $g_{12}(r)$.

Figure 4e–h displays $g(r)$ for near equimolar mixtures varied in σ from 1.29 to 1.95. To probe how σ affects mixture

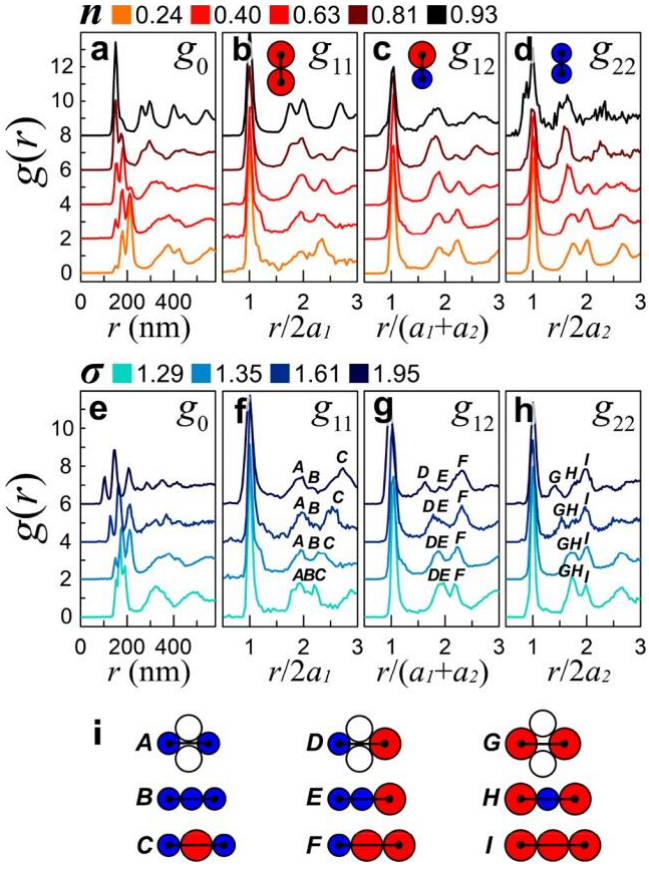

Figure 4. Radial distribution functions $g(r)$ for bidisperse NP mixtures. Functions $g_0(r)$, $g_{11}(r)$, $g_{12}(r)$, and $g_{22}(r)$ plotted for (a–d) n varied with σ fixed at 1.35 and (e–h) σ varied with n fixed at ≈0.50. (i) Sphere arrangements associated with the peaks A–H indicated in plots (f)–(h). Functions have been vertically shifted for clarity.

https://dx.doi.org/10.1021/acsnano.0c04682
ACS Nano 2020, 14, 10589–10599

disorder, the packing arrangements associated with the main peaks (after the peaks of NP contacts) of $g_{11}(r)$, $g_{12}(r)$, and

https://dx.doi.org/10.1021/acsnano.0c04682
ACS Nano 2020, 14, 10589−10599

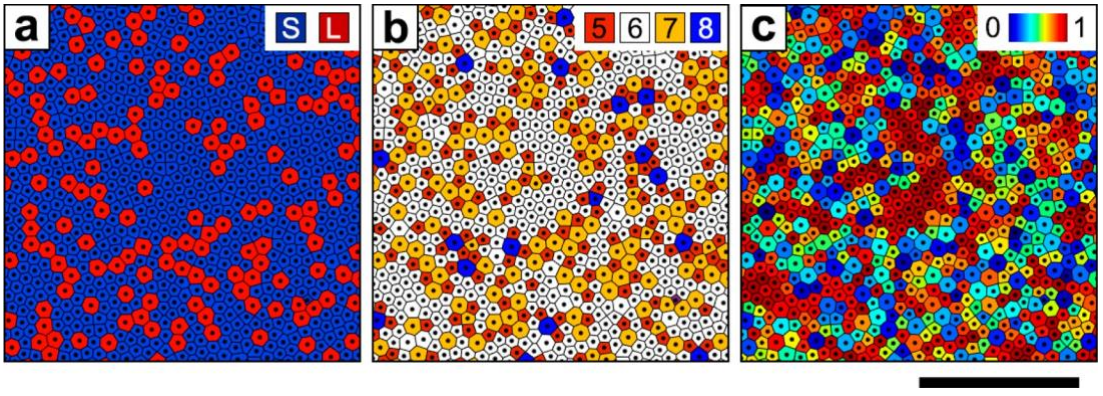

Figure 5. Local order metrics for a bidisperse NP packing. Voronoi cells are colorized by (a) a, (b) z, and (c) $|\psi_6|$. Scale bar is 2 μm, and σ = 1.35 and n = 0.81.

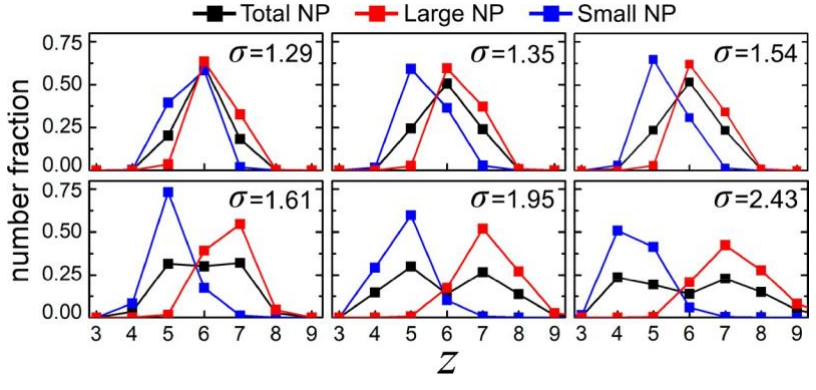

Figure 6. Distributions of z for $n \approx 0.5$ at different σ. Top row (left to right): n = 0.47, 0.40, and 0.34. Bottom row (left to right): n = 0.42, 0.50, and 0.46. z is calculated for total (black), large (red), and small (blue) NP centers.

$g_{22}(r)$ are sketched in Figure 4i. The positions of sketched peaks corresponded to $r \sim 250-450$ nm in Figure 4e. When $g(r)$ is plotted against appropriately scaled r, as done in Figure 4f−h, well separated $g(r)$ peaks at large σ converge into just two peaks as σ falls toward unity; the scaled peak positions in this limit are √3 and √4, as anticipated from the sketches in Figure 4i. While peaks of Figure 4f−h are better separated at larger σ, they are also broadened due to increased disorder. The same trend is shown in Figure 4e, which plots $g_0(r)$ *vs* unscaled r, with peaks observed to split and weaken as σ increases. Diverse packing topologies attenuated the integrated peak intensity in $g_0(r)$.

The orientational or hexagonal order parameter ψ_6 is calculated for NP k at position r_k from the set of angles θ_{kj} constructed between an arbitrary but *fi*xed axis and lines drawn through the NP and each of its n_b nearest neighbors,[33]

$$\psi_6(r_k) = \frac{1}{n_b}\sum_{j \in N_k} e^{6i\theta_{kj}}$$

A schematic of θ_{kj} is provided in Figure S7. Nearest neighbor NPs are identi*fi*ed by radical Voronoi tessellation, and i is the imaginary unit. The magnitude of ψ_6, ranging from zero to unity, provides a measure of the degree of local hexagonal order at r_k, and the average of this magnitude over all NPs, designated Ψ_6, provides a measure of the average degree of local hexagonal order across the system. Figure 3c demonstrates that Ψ_6 for the mixture of Figure 3a is ~0.53, a modest far from perfect. The spatial persistence of hexagonal order is captured in the Ψ_6 correlation function

$$g_6(r) = \mathrm{Re}\{\langle \psi_6^*(\mathbf{r}_k)\psi_6(\mathbf{r}_l)\rangle_{|\mathbf{r}_k-\mathbf{r}_l|=r}\}$$

where the average is over NP pairs (k,l) satisfying the condition $|r_k - r_l| = r$. Figure S8 shows that $g_6(r)$ for the mixture in Figure 3a decays approximately exponentially with a characteristic decay length ~$2.4a_1$. Such decay is typical of an isotropic hard sphere *fl*uid maintaining only local orientational order.[34]

The translational order metric T^*, derived from $g_0(r)$, summarizes information about local correlations in the radial position of a sphere packing,[25]

$$T^* = \frac{\int_{2a_1}^{r_c} |g_0(r) - 1| dr}{r_c - 2a_1}$$

where r_c is a cuto*ff* distance, chosen as $3\rho^{-0.5}$ (ρ is the areal value indicating the visually obvious, that hexagonal packing is

https://dx.doi.org/10.1021/acsnano.0c04682
ACS Nano 2020, 14, 10589−10599

number density of NPs). For this choice, T^* quantifies the degree to which packing departs from random, *i.e.*, is characterized by $g_0(r) \neq 1$, on a scale of ~4 NP diameters; $T^* \sim 0$ for a fluidlike configuration and ~1.5 for a crystal. The mixture of Figure 3a displays modest radial organization, signified by the departure of T^* from zero in Figure 3c ($T^* \approx 0.35$). Magnitudes of these order metrics suggest that the packing of Figure 3a approximates the ensemble average of the bidisperse disordered packing ($\sigma = 1.40$, $n = 0.50$) calculated by Atkinson *et al.*[25] The same orders metrics will be provided for other packing conditions in a subsequent section.

https://dx.doi.org/10.1021/acsnano.0c04682
ACS Nano 2020, 14, 10589−10599

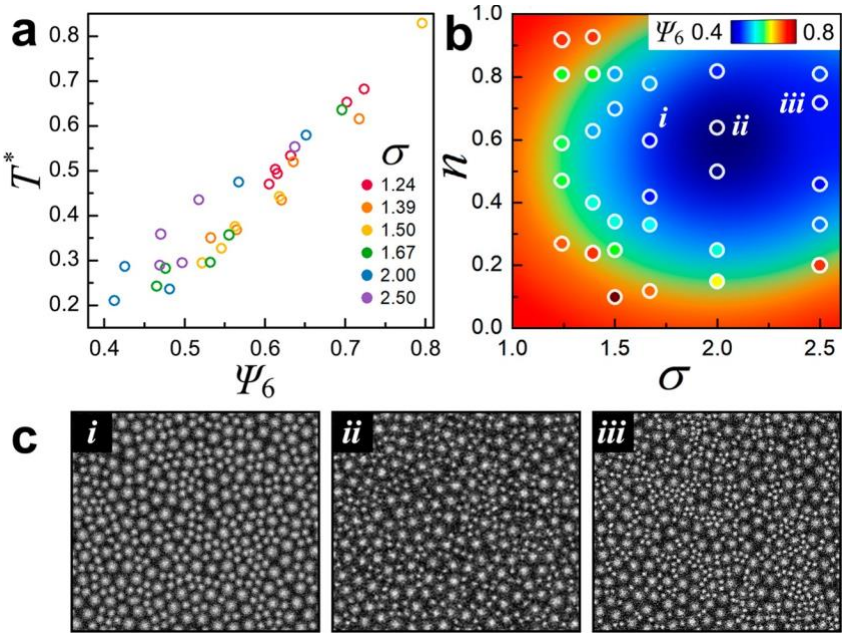

Figure 7. (a) Correlation of T* and Ψ_6. (b) Map of Ψ_6 as a function of n and σ. (c) Jammed NPs at the σ and n pairings labeled in (b). better mixed small and large NPs display distinctly lower $|\psi_6|$

Nearest Neighbor Statistics. For a 2D crystal in which monodisperse spheres predominantly pack onto a triangular lattice with six nearest neighbors, defects are typically described as disclinations, nearest neighbor numbers other than six, or dislocations, bound pairs of *five*-coordinated and seven-coordinated disclinations.[35] The jammed NPs of this study were not monodisperse, and in most instances they did not regularly pack into a de*fi*ned lattice, making such "defect" descriptions ambiguous. Nevertheless, radical tessellation assigns z nearest neighbors to each large or small NP. In Figure 5a, a jammed NP packing with $\sigma = 1.35$ and $n = 0.82$ has been colorized according to NP radius, and in Figure 5b NPs have been recolorized according to z, which ranged from *fi*ve to eight. Nearly half of the NPs in Figure 5b have z other than six, making assignment of disclinations and dislocations problematic. Figure 6 displays histograms of z for small, large, and all NPs for $n \approx 0.5$ packings prepared at di*ff*erent σ. As σ increases, the NP fraction with $z = 6$ decreases in correspondence with increases in the fractions with larger and smaller z. The *fi*gure also shows that more NPs tend to surround larger NPs than smaller NPs, a straightforward outcome, and that the breadths of all three z distributions grow with increasing σ, revealing growing disorder. All packings were hyperstatic with mean $z \sim 6$, having more contacts between NPs than those minimally required for collective jamming (isostatic packing, mean $z \sim 4$).[36]

Surveying Figure 5a and b, small NPs with $z = 6$ are seen to reside preferentially in compact, interconnected, and somewhat ordered regions containing ten or more NPs, while both small and large NPs with $z \neq 6$ concentrate in the relatively disordered areas in between. The *fi*rst image also hints that large NPs can assemble as short, irregular strings; when n is slightly smaller, as in Figure 3a, the now more continuous strings seem to percolate. In Figure 5c, the same packing is colorized according to $|\psi_6|$.[33] The new images highlight essentially the same regions evident in Figure 5a, demonstrating that spatial patterns of mixing/demixing mostly mirror spatial patterns of order/disorder. The disordered regions of

https://dx.doi.org/10.1021/acsnano.0c04682
ACS Nano 2020, 14, 10589−10599

(~0.2) than the small NP-rich ordered domains (~0.8), and the latter adopt lattices of well-defined orientation..

As previously explained, Ψ_6 and T^* manifest distinct aspects of structure evaluated at different local length scales. Nevertheless, as demonstrated in Figure 7a, the two metrics are strongly correlated: when plotted against each other over a spread of σ, a line without systematic deviations emerges. For simulated monodisperse jammed 2D disk packings, Torquato *et al.* obtained a similar correlation and suggested that Ψ_6 and T^* serve as essentially equivalent measures of local order.[26] This correlation is rooted in the way that order propagates upward from nearest neighbors. For a 2D jammed sphere/disk packing, hexagonal local cells interlock with each other so that they cannot rotate relative to each other enough to release much short-range positional order; orientational and positional orders over the scale of few NP diameters are thereby reinforced. The same connection is missing in analogous lower density unjammed systems, for which uncoupled local orientational and positional order are displayed. Although the two metrics are nearly proportional for the σ range examined, further work will be necessary to determine if linearity extends to larger σ.

Order Metrics Mapped against NP Composition and Size Ratio. Figure 7b presents a 2D map of n and σ dependences of Ψ_6. Each point, colored according to average Ψ_6, combines analysis of several independent images. The analogous T^* map, displayed as Figure S9, is similar, a consequence of the close correlation between T^* and Ψ_6. The global minimum of Ψ_6 is at $\sigma \approx 2.0$ and $n \approx 0.6$, where Ψ_6 is noticeably less ($\Psi_6 \approx 0.42$) than for a mixture at $\sigma = 1.4$ and $n = 0.5$ ($\Psi_6 \approx 0.53$), a condition cited in the literature for its high disorder. Figure 2 provides SEM images for several n and σ pairings plotted on the Ψ_6 map. For the images of Figure 2a, c, and d, $\Psi_6 \approx 0.58-0.60$ and each image visually hints of limited local order, while for the images of Figure 2e and f, $\Psi_6 \approx 0.40-0.42$ and nowhere is significant local order discerned. Figure 2b, corresponding to the analyses summarized in Figures 3 and 5, offers an intermediate case, one for which local order is visually ambiguous. At the largest σ of Figure 2,

https://dx.doi.org/10.1021/acsnano.0c04682
ACS Nano 2020, 14, 10589−10599

(Figure 2f, σ = 1.95), defects in the form of empty rings containing five to seven NPs are observed.

Inspecting Figures 2 and 7b, one might surmise that disorder grows monotonically with σ at large σ ($\gtrsim$1.35), at least for near evenly mixed NP compositions at which disorder is greatest. Deeper study of Figure 7b for these mixed compositions reveals that Ψ_6 begins to drop at large σ ($\gtrsim$2.0), indicating an intermediate maximum of disorder. Seeking to interpret the turnaround in terms of NP configurations, images from below, near, and above the suggested $\sigma \approx 2.0$ transition are presented in Figure 7c, corresponding to the conditions labeled *i*, *ii*, and *iii* in Figure 7b. The raised order at condition *iii* clearly reflects small NPs clustering in irregular gaps between large NPs; these gaps are typically larger than the interstitial areas defined by large NPs in mutual contact. At larger scales, the system seems randomly mixed. Despite the difference of conditions, the small NP clusters in Figure 7c are not entirely different than those seen in Figure 5, although their local order is less. Figure 7b, corresponding to condition *ii*, has the lowest Ψ_6 of the three conditions compared, and the number of empty ring defects is largest. With such unequal NP sizes, other measures of order/disorder, such as departures from z = 6 (Figure 6) are less insightful, especially in understanding how these measures trend with σ. For all σ examined, Ψ_6 decreased as n approaches ~0.5, revealing greater disorder of equimolar mixtures.

Depletion Interactions. As NPs were attached to the liquid surface prior to jamming, they had ample opportunity to rearrange under expanding NP interactions. Mixing could thereby manifest not just the local structural constraints of jamming but also the thermodynamics of mixing, and most particularly, the entropy of mixing of different-sized components. The latter can generate depletion attractions between like-sized components, possibly causing demixing or crystallization, i.e., fluid−fluid or fluid−solid phase separation.[29,30] At short length scales, the packing implications of structural and depletion effects are not entirely distinct. For 2D bidisperse hard spheres, whether depletion-induced phase separation is favored for particular combinations of ϕ, n, and σ remains an open question, and even if favored jamming could kinetically arrest the process at intermediate stages, providing clusters rather than macroscopic phases. For relatively dilute hard spheres in 3D dispersions, experimental investigators reported depletion-induced phase separation (crystallization)at σ as small as 2,[37] and several theories and simulations suggest that phase separation in higher density mixtures is general.[38] However, we are unaware of depletion interactions being studied at densities near jamming in either 2D or 3D, and many investigations have addressed only the pairwise interaction of two large spheres in a low density sea of small spheres, *i.e.*, interactions in the limit of high n and low ϕ.[39] Two experimental studies found that 2D bidisperse hard sphere/disk mixtures can display clustering under weak depletion interactions.[40]

To assess the role of depletion interactions for the current NP monolayers, the "effective" in-plane pair interaction potential $U_{22,\mathrm{eff}}(r)$ for large NPs was calculated from the Boltzmann equation $U_{22,\mathrm{eff}}(r) = -k_B T \ln[g_{22}(r)]$ over $0 \leq (r - 2a_2)/2a_1 \leq 1$.[41] $U_{22,\mathrm{eff}}(r)$ can be considered analogous to a potential of mean force reflective of clustering under multibody interactions. However, since these jammed systems depart from equilibrium, caution is advised when $U_{22,\mathrm{eff}}(r)$ is referenced as a potential. Given the significant fraction of large NPs, $U_{22,\mathrm{eff}}(r)$ is not a quantitative reflection of the

https://dx.doi.org/10.1021/acsnano.0c04682
ACS Nano 2020, 14, 10589−10599

interactions between two large NPs but indicates that large NPs are clustered as a result of multibody interactions. For the differences in ϕ at jamming, the differing breadths of radius distribution between NP samples, and the limited ability of the monolayers to equilibrate, $U_{22,\mathrm{eff}}(r)$ must be viewed with caution when comparing trends at different conditions or comparing experiment to theory/simulation. Figure 8a shows

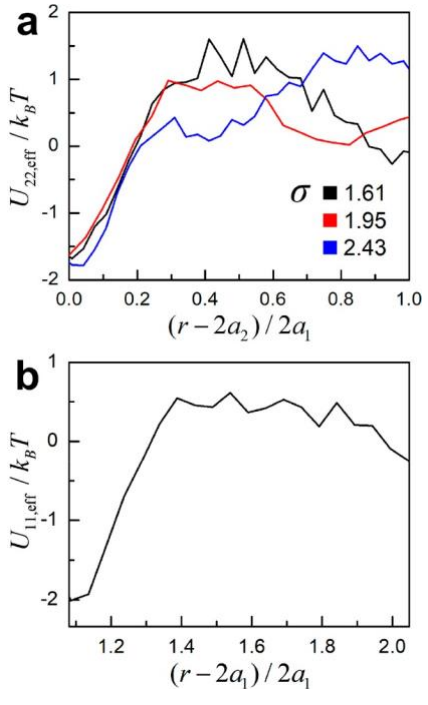

Figure 8. Effective interaction potential of NPs in dense mixtures. (a) Interaction between large NPs. Packing conditions are same to those in Figure 7c. (b) Interactions between small NPs for $\sigma = 2.43$ and $n = 0.72$, same conditions as *iii* in Figure 7c.

$U_{22,\mathrm{eff}}(r)$ for the mixtures depicted in images *i*, *ii*, and *iii* of Figure 7c. Although the full images are larger than shown, the data are still noisy due to limited statistics. However, a clear short-range attractive energy of about $\sim -1.7\ k_BT$ is noted for each σ. This energy and the form of $U_{22,\mathrm{eff}}(r)$ are reasonably consistent with the theoretical results of Perera-Burgos *et al.*,[15] who calculated $U_{22,\mathrm{eff}}(r)$ for modestly dense, bidisperse ($\sigma = 5$)2D sphere packings by solving the Ornstein−Zernike equation with the Percus−Yevick closure relationship. For the largest experimental size ratio ($\sigma = 2.43$), image *iii* suggests that depletion interactions between the large NPs are accompanied by significant attractive interactions between the small NPs, which are seen to preferentially segregate to gaps between large NPs, assembling into irregular clusters containing from ~3 to ~10 small NPs; the clusters have characteristic dimensions of ~1 to ~3 small NP diameters, suggesting a weak layering of the small NPs between the large NPs, as predicted by previous simulations.[38,39,42] Figure 8b displays the effective interaction potential $U_{11,\mathrm{eff}}(r)$ between small NPs for the experimental conditions of image *iii*. A minimum of $\sim -2\ k_BT$ is noted for small NPs nearly in contact.[15]

At fixed n, NP clustering becomes more evident as σ increases, a trend that the images in Figure 7b make clear. This clustering explains the increased local order determined for $n \approx 0.5$ mixtures as σ grows beyond ~2. Above this threshold, longer range [$r > 2(a_1 + a_2)$] oscillations in $U_{22,\mathrm{eff}}(r)$ become

https://dx.doi.org/10.1021/acsnano.0c04682
ACS Nano 2020, 14, 10589−10599

more pronounced, hinting that under depletion attractions the large NPs locally assemble with some crystalline order. This order is only subtly revealed when images *ii* (σ = 1.95) and *iii* (σ = 2.43) are visually compared. We could not determine whether the clustering is an equilibrium phenomenon or the result of macroscopic phase separation that is kinetically arrested by jamming.

The 2D organization of bidisperse NPs on an open liquid interface was monitored in this project by a nanoscale electron microscopy method that o*ff*ered single particle imaging over surface areas encompassing thousands of densely packed NPs. Compared to previous microscopy approaches for the study of jammed 2D spheres/disks, this method had advantages in terms of (i) access to nearly ideal particle−particle interactions (close to hard spheres), (ii) the ability to observe well-dispersed particle mixtures in a well-de*fi*ned plane, (iii) high resolution (positions tracked to nanometer accuracy), (iv) signi*fi*cant particle mobility prior to jamming, and (v) notable absence of imaging artifacts (charging, loss of contrast with time, imaging interference from bulk particles, *etc*.). Consequently, the jammed layers possessed well-de*fi*ned and easily reproduced packing statistics, which in this study, were characterized for both local order and local mixing. The method had a few downsides: (i) bidispere sphere packing was not perfectly 2D and (ii) sphere−sphere contacts were not directly imaged. These limitations played little role here. As will be described in a separate publication, *in situ* SEM admits precise single particle tracking of unjammed or nearly jammed spheres for an hour or longer, more than needed to attain statistically well-controlled and disordered jamming. Thus, a single NP understanding of how these layers formed is accessible.

Absent comparable experimental studies, the 2D jamming results for bidisperse spheres reported here basically a*ffi*rm previous theory/simulation works. Most notably, the prediction of high disorder in appropriately designed mixtures was veri*fi*ed in a technologically relevant context, NPs jammed on a liquid interface. Open questions remain concerning packing order/disorder trends observed at $\sigma \gtrsim 1.4$, the putative ideal choice for achieving greatest disorder in a 2D sphere/disk packing. While experimentally observed disorder had a maximum with respect to σ, the maximum was shifted to $\sigma \approx 2.0$, and the physical underpinnings of this maximum may not be the same as those leading to the maximum noted by simulation; most likely, increased ordering at higher σ arises from depletion interactions.

The current analyses also addressed the degree of local mixing. The mixture composition in the region surrounding a test sphere did not reach its bulk value until radial distances equivalent to 10−20 sphere shells, and the local arrangement of spheres of one size at this scale did not seem random for many combinations of n and σ. The local mixing issue was most pronounced at high σ, where for $n \approx 0.5$, a clear local clustering of small spheres was seen in the spaces between large spheres. Clustering might be attributed to growing composition *fl*uctuations upon approach to depletion-induced phase separation or, alternately, by the quenching by jamming of macroscopic phase separation. Future studies that record the time dependence of mixing and ordering upon approach to jamming should resolve this issue.

https://dx.doi.org/10.1021/acsnano.0c04682
ACS Nano 2020, 14, 10589−10599

CONCLUSIONS

Jammed bidisperse NP sphere packings on an IL surface were characterized by an *in situ* SEM imaging method made feasibleby IL nonvolatility. Due to large NP binding energies, dense and nearly irreversibly attached Gibbs NP monolayers formed spontaneously from bulk-dispersed PEGylated silica NPs, and during surface assembly, high in-plane NP mobility and weak NP interactions led to well-produced, highly uniform disordered packings. Packing order was characterized by measures such as $g(r)$, Ψ_6, T^*, and z, all of which confirmedthat σ in the range 1.5−2.0 maximized disorder at intermediate n. Mixing was not uniform over surprisingly large but still local length scales, reflecting a combination of structural and depletion interactions. Results are in general accord with existing theory/simulation predictions for order/disorder and mixing in 2D packings of bidisperse hard spheres/disks. The experimental methods outlined here are ideally suited to time-dependent single particle tracking examinations ("movies") of jamming and other nanoscale assembly processes on liquid surfaces.

MATERIALS AND METHODS

Sample Preparation. Amine-functionalized silica NPs of 80 ± 6, 100 ± 5, 121 ± 7, 144 ± 11, 187 ± 6, and 195 ± 8 nm diameter were purchased from Nanocomposix. To disperse the NPs in IL and direct their hard sphere packing at IL surfaces, 5000 g/mol PEG ligands were covalently attached by a condensation reaction between PEG succinimidyl ester end-groups and NP surface amines. Procedures and material sources are provided in the Supporting Information. After PEGylation, the NPs were dialyzed against ethanol for several days. Ethanolic NP dispersions of different σ were then mixed in a microcentrifuge tube at the targeted n, and five to six cycles of centrifugation and washing with methanol were applied to remove soluble contaminants, particularly unattached PEG. In the last washing, the methanol-dispersed NPs were concentrated to ~20 mg/mL and agitated thoroughly for 30 min by vortex mixing and sonication.

After a NP dispersion was mixed and purified, SEM specimens were prepared by first depositing a 4 μL droplet of pure IL onto a precleaned 1 cm square P-type conductive silicon wafer (boron-doped, 0.001−0.005 Ω·cm, Silicon Prime Wafers), chosen to minimize specimen charging. The IL, 1-ethyl-3-methylimidazolium ethylsulfate ([EMIM][$EtSO_4$], 99% purity), was purchased from Iolitech and used without purification. On the droplet surface, 3 μL of a methanolic mixed NP dispersion was carefully spread, and immediately afterward the liquids mixed near the surface even as the methanol rapidly evaporated (a few minutes). With methanol removed, the bulk dispersed NPs began to segregate to the IL surface, forming a monolayer that increased in areal density over tens of minutes and reached saturation after several hours. Any NPs beyond those needed to form the monolayer remained in the IL bulk. To remove residual methanol and water traces absorbed from the atmosphere (the IL is hygroscopic), each specimen was placed in a vacuum oven for at least 1 h before SEM examination.

SEM Imaging and Data Analysis. Imaging was performed using a FEI Magellan XHR 400 FE-SEM at 3 kV acceleration voltage and 13pA beam current to minimize beam damage. Each scan produced a1536 × 1024 pixel image, and magnification was selected such that the nominal NP diameter spanned 12 or more pixels while an individual image captured >8000 NPs. The raw grayscale images were filtered with a Gaussian blur to reduce noise and then transformed into binary images by thresholding. Neighboring NPs that appeared to fuse upon binarization were separated by a modified watershed algorithm. Centroids of the bright NP "circles" distributed across each image were taken as NP positions in packing analyses. To distinguish NPs ofdifferent diameter, a histogram of NP areas was created for each image, and NP areas above and below the histogram's central

https://dx.doi.org/10.1021/acsnano.0c04682
ACS Nano 2020, 14, 10589−10599

minimum were sorted into separate bins. Radical Voronoi tessellations were made for each particle configuration to assign NP neighbors unambiguously.[43] The 2D pair correlation function $g(r)$ was computed as the areal number density of NPs at a center-to-center distance between r and $r + dr$ normalized by the average NP number density across the image.

ASSOCIATED CONTENT

Supporting Information

The Supporting Information is available free of charge at https://pubs.acs.org/doi/10.1021/acsnano.0c04682.

Procedures for the grafting of PEG onto silica NPs; growth of a NP monolayer at different drop ages; effective radii of NPs at small-large NP contacts; uniform n and ϕ over different locations on the interface; shell number S defined by radical Voronoi tessellation; normalized distribution of local n with varying cluster size S calculated for $\sigma = 1.35$ and $n = 0.63$; distribution of local n fitted with the probability density function of a normal distribution for $S = 3$, 6, and $9/\sigma = 1.35$ and $n = 0.63$; schematic of bond angle θ_{kj} for calculation of the bond-orientation order parameter ψ_6; correlation function g_6 for $\sigma = 1.35$ and $n = 0.63$; map of T^* as a function of n and σ (PDF)

AUTHOR INFORMATION

Corresponding Authors

Thomas P. Russell − *Department of Polymer Science and Engineering, University of Massachusetts Amherst, Amherst, Massachusetts 01003, United States; Materials Sciences Division, Lawrence Berkeley National Laboratory, Berkeley, California 94720, United States; Beijing Advanced Innovation Center for Soft Matter Science and Engineering, Beijing University of Chemical Technology, Beijing 100029, China; Advanced Institute for Materials Research (WPI-AIMR), Tohoku University, Sendai 980-8577, Japan;* orcid.org/0000-0001-6384-5826; Email: russell@mail.pse.umass.edu

David A. Hoagland − *Department of Polymer Science and Engineering, University of Massachusetts Amherst, Amherst, Massachusetts 01003, United States*; Email: hoagland@mail.pse.umass.edu

Authors

Yige Gao − *Department of Polymer Science and Engineering, University of Massachusetts Amherst, Amherst, Massachusetts 01003, United States*

Paul Y. Kim − *Materials Sciences Division, Lawrence Berkeley National Laboratory, Berkeley, California 94720, United States;* orcid.org/0000-0002-7271-0568

Complete contact information is available at: https://pubs.acs.org/10.1021/acsnano.0c04682

Author Contributions

⊥Y.G. and P.Y.K. contributed equally to the research, which was directed by D.A.H. and T.P.R.

Notes

The authors declare no competing financial interest.

ACKNOWLEDGMENTS

We acknowledge the financial support of the National Science Foundation through DMR-1807255.

REFERENCES

(1) Liu, A. J.; Nagel, S. R. Jamming Is Not Just Cool Any More. *Nature* 1998, *396*, 21−22.

(2) Cates, M. E.; Wittmer, J. P.; Bouchaud, J. P.; Claudin, P. Jamming, Force Chains, and Fragile Matter. *Phys. Rev. Lett.* 1998, *81*, 1841−1844.

(3) Forth, J.; Kim, P. Y.; Xie, G.; Liu, X.; Helms, B. A.; Russell, T. P. Building Reconfigurable Devices Using Complex Liquid−Fluid Interfaces. *Adv. Mater.* 2019, *31*, 1806370.

(4) Donev, A.; Cisse, I.; Sachs, D.; Variano, E. A.; Stillinger, F. H.; Connelly, R.; Torquato, S.; Chaikin, P. M. Improving the Density of Jammed Disordered Packings Using Ellipsoids. *Science* 2004, *303*, 990−993.

(5) Xu, X.; Rice, S. A. Maximally Random Jamming of One-Component and Binary Hard-Disk Fluids in Two Dimensions. *Phys. Rev. E* 2011, *83*, 021120.

(6) Huerta, A.; Carrasco-Fadanelli, V.; Trokhymchuk, A. Towards Frustration of Freezing Transition in a Binary Hard-Disk Mixture. *Condens. Matter Phys.* 2012, *15*, 43604.

(7) Hoffmann, N.; Ebert, F.; Likos, C. N.; Löwen, H.; Maret, G. Partial Clustering in Binary Two-Dimensional Colloidal Suspensions. *Phys. Rev. Lett.* 2006, *97*, 078301.

(8) Kollmann, M.; Hund, R.; Rinn, B.; Nägle, G.; Zahn, K.; König, H.; Maret, G.; Klein, R.; Dhont, J. K. G. Structure and Tracer-Diffusion in Quasi−Two-Dimensional and Strongly Asymmetric Magnetic Colloidal Mixtures. *Europhys. Lett.* 2002, *58*, 919−925.

(9) Keim, N. C.; Arratia, P. E. Role of Disorder in Finite-Amplitude Shear of a 2D Jammed Material. *Soft Matter* 2015, *11*, 1539−1546.

(10) Bocquet, L.; Hansen, J. P.; Biben, T.; Madden, P. Amorphization of a Substitutional Binary Alloy: A Computer 'Experiment'. *J. Phys.: Condens. Matter* 1992, *4*, 2375−2387.

(11) Perera, D. N.; Harrowell, P. Stability and Structure of a Supercooled Liquid Mixture in Two Dimensions. *Phys. Rev. E: Stat. Phys., Plasmas, Fluids, Relat. Interdiscip. Top.* 1999, *59*, 5721−5743.

(12) Speedy, R. J. Random Jammed Packings of Hard Discs and Spheres. *J. Phys.: Condens. Matter* 1998, *10*, 4185−4194.

(13) Russo, J.; Romano, F.; Tanaka, H. Glass Forming Ability in Systems with Competing Orderings. *Phys. Rev. X* 2018, *8*, 021040.

(14) Koeze, D. J.; Vågberg, D.; Tjoa, B. B. T.; Tighe, B. P. Mapping the Jamming Transition of Bidisperse Mixtures. *Europhys. Lett.* 2016, *113*, 54001.

(15) Perera-Burgos, J. A.; Méndez-Alcaraz, J. M.; Pérez-Ángel, G.; Castañeda-Priego, R. Assessment of the Micro-Structure and Depletion Potentials in Two-Dimensional Binary Mixtures of Additive Hard-Disks. *J. Chem. Phys.* 2016, *145*, 104905.

(16) Kim, P. Y.; Gao, Y.; Chai, Y.; Ashby, P. D.; Ribbe, A. E.; Hoagland, D. A.; Russell, T. P. Assessing Pair Interaction Potentials of Nanoparticles on Liquid Interfaces. *ACS Nano* 2019, *13*, 3075−3082.

(17) Forth, J.; Liu, X.; Hasnain, J.; Toor, A.; Miszta, K.; Shi, S.; Geissler, P. L.; Emrick, T.; Helms, B. A.; Russell, T. P. Reconfigurable Printed Liquids. *Adv. Mater.* 2018, *30*, 1707603.

(18) Jin, D.; Xi, P.; Wang, B.; Zhang, L.; Enderlein, J.; van Oijen, A. M. Nanoparticles for Super-Resolution Microscopy and Single-Molecule Tracking. *Nat. Methods* 2018, *15*, 415−423.

(19) Saxton, M. J.; Jacobson, K. Single-Particle Tracking:Applications to Membrane Dynamics. *Annu. Rev. Biophys. Biomol. Struct.* 1997, *26*, 373−399.

(20) de Jonge, N.; Ross, F. M. Electron Microscopy of Specimens in Liquid. *Nat. Nanotechnol.* 2011, *6*, 695.

(21) Kim, P. Y.; Ribbe, A. E.; Russell, T. P.; Hoagland, D. A. Visualizing the Dynamics of Nanoparticles in Liquids by Scanning Electron Microscopy. *ACS Nano* 2016, *10*, 6257−6264.

(22) Egerton, R. F.; Li, P.; Malac, M. Radiation Damage in the Tem and Sem. *Micron* 2004, *35*, 399−409.

(23) Plumere, N.; Ruff, A.; Speiser, B.; Feldmann, V.; Mayer, H. A. Stöber Silica Particles as Basis for Redox Modifications: Particle Shape, Size, Polydispersity, and Porosity. *J. Colloid Interface Sci.* 2012, *368*, 208−219.

https://dx.doi.org/10.1021/acsnano.0c04682
ACS Nano 2020, 14, 10589−10599

(24) Jokerst, J. V.; Lobovkina, T.; Zare, R. N.; Gambhir, S. S. Nanoparticle Pegylation for Imaging and Therapy. *Nanomedicine (London, U. K.)* 2011, *6*, 715−728.
(25) Atkinson, S.; Stillinger, F. H.; Torquato, S. Existence of Isostatic, Maximally Random Jammed Monodisperse Hard-Disk Packings. *Proc. Natl. Acad. Sci. U. S. A.* 2014, *111*, 18436−18441.
(26) Torquato, S.; Truskett, T. M.; Debenedetti, P. G. Is Random Close Packing of Spheres Well Defined? *Phys. Rev. Lett.* 2000, *84*, 2064−2067.
(27) Speedy, R. J. Glass Transition in Hard Disc Mixtures. *J. Chem. Phys.* 1999, *110*, 4559−4565.
(28) Zachary, C. E.; Jiao, Y.; Torquato, S. Hyperuniformity, Quasi-Long-Range Correlations, and Void-Space Constraints in Maximally Random Jammed Particle Packings. Ii. Anisotropy in Particle Shape. *Phys. Rev. E* 2011, *83*, 051309.
(29) Kaplan, P. D.; Rouke, J. L.; Yodh, A. G.; Pine, D. J. Entropically Driven Surface Phase Separation in Binary Colloidal Mixtures. *Phys. Rev. Lett.* 1994, *72*, 582−585.
(30) Biben, T.; Hansen, J.-P. Phase Separation of Asymmetric Binary Hard-Sphere Fluids. *Phys. Rev. Lett.* 1991, *66*, 2215−2218.
(31) Newhall, K. A.; Pontani, L. L.; Jorjadze, I.; Hilgenfeldt, S.; Brujic, J. Size-Topology Relations in Packings of Grains, Emulsions, Foams, and Biological Cells. *Phys. Rev. Lett.* 2012, *108*, 268001.
(32) Samuels, M. L.; Witmer, J. A. *Statistics for the Life Sciences*, 3rd ed.; Prentice Hall: Upper Saddle River, NJ, 2003.
(33) Nelson, D. R. *Bond-Orientational Order in Condensed Matter Systems*, 1st ed.; Springer-Verlag: New York, 2011.
(34) Kelleher, C. P.; Guerra, R. E.; Hollingsworth, A. D.; Chaikin, P. M. Phase Behavior of Charged Colloids at a Fluid Interface. *Phys. Rev. E: Stat. Phys., Plasmas, Fluids, Relat. Interdiscip. Top.* 2017, *95*, 022602.
(35) Qi, W.; Gantapara, A. P.; Dijkstra, M. Two-Stage Melting Induced by Dislocations and Grain Boundaries in Monolayers of Hard Spheres. *Soft Matter* 2014, *10*, 5449−5457.
(36) Donev, A.; Torquato, S.; Stillinger, F. H. Pair Correlation Function Characteristics of Nearly Jammed Disordered and Ordered Hard-Sphere Packings. *Phys. Rev. E* 2005, *71*, 011105.
(37) Dinsmore, A. D.; Yodh, A. G.; Pine, D. J. Phase Diagrams of Nearly-Hard-Sphere Binary Colloids. *Phys. Rev. E: Stat. Phys., Plasmas, Fluids, Relat. Interdiscip. Top.* 1995, *52*, 4045−4057.
(38) López-Sánchez, E.; Estrada-Alvarez, C. D.; Pérez-Angel, G.; Méndez-Alcaraz, J. M.; González-Mozuelos, P.; Castañeda-Priego, R. Demixing Transition, Structure, and Depletion Forces in Binary Mixtures of Hard-Spheres: The Role of Bridge Functions. *J. Chem. Phys.* 2013, *139*, 104908.
(39) Castañeda-Priego, R.; Rodríguez-López, A.; Méndez-Alcaraz, J. M. Depletion Forces in Two-Dimensional Colloidal Mixtures. *J. Phys.: Condens. Matter* 2003, *15*, S3393−S3409.
(40) Melby, P.; Prevost, A.; Egolf, D. A.; Urbach, J. S. Depletion Force in a Bidisperse Granular Layer. *Phys. Rev. E* 2007, *76*, 051307.
(41) Behrens, S. H.; Grier, D. G. Pair Interaction of Charged Colloidal Spheres near a Charged Wall. *Phys. Rev. E: Stat. Phys., Plasmas, Fluids, Relat. Interdiscip. Top.* 2001, *64*, 050401.
(42) Thorneywork, A. L.; Roth, R.; Aarts, D. G. A. L.; Dullens, R. P. A. Communication: Radial Distribution Functions in a Two-Dimensional Binary Colloidal Hard Sphere System. *J. Chem. Phys.* 2014, *140*, 161106.
(43) Gellatly, B. J.; Finney, J. L. Characterisation of Models of Multicomponent Amorphous Metals: The Radical Alternative to the Voronoi Polyhedron. *J. Non-Cryst. Solids* 1982, *50*, 313−329.

https://dx.doi.org/10.1021/acsnano.0c04682
ACS Nano 2020, 14, 10589−10599